

Bottom-Up Assembly of Colloidal Gold and Silver Nanostructures for Designable Plasmonic Structures and Metamaterials

Shangjr Gwo,^{*,†,‡} Meng-Hsien Lin,[†] Chieh-Lun He,[‡] Hung-Ying Chen,[†] and Toshiharu Teranishi^{§,||}

[†]Department of Physics, National Tsing-Hua University, Hsinchu 30013, Taiwan

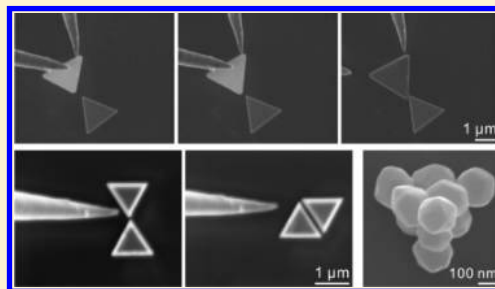
[‡]Institute of Nanoengineering and Microsystems, National Tsing-Hua University, Hsinchu 30013, Taiwan

[§]Institute for Chemical Research, Kyoto University, Gokasho, Uji, Kyoto 611-0011, Japan

^{||}CREST, Japan Science and Technology Agency (JST), 1-1-1 Tennodai, Tsukuba, Ibaraki 305-8571, Japan

ABSTRACT: We report on bottom-up assembly routes for fabricating plasmonic structures and metamaterials composed of colloidal gold and silver nanostructures, such as nanoparticles (“metatoms”) and shape-controlled nanocrystals. Owing to their well-controlled sizes/shapes, facile surface functionalization, and excellent plasmonic properties in the visible and near-infrared regions, these nanoparticles and nanocrystals are excellent building blocks of plasmonic structures and metamaterials for optical applications. Recently, we have utilized two kinds of bottom-up techniques (i.e., multiple-probe-based nanomanipulation and layer-by-layer self-assembly) to fabricate strongly coupled plasmonic dimers, one-dimensional (1D) chains, and large-scale two-dimensional/three-dimensional (2D/3D) nanoparticle supercrystals.

These coupled nanoparticle/nanocrystal assemblies exhibit unique and tunable plasmonic properties, depending on the material composition, size/shape, intergap distance, the number of composing nanoparticles/nanocrystals (1D chains), and the nanoparticle layer number in the case of 3D nanoparticle supercrystals. By studying these coupled nanoparticle/nanocrystal assemblies, the fundamental plasmonic metamaterial effects could be investigated in detail under well-prepared and previously unexplored experimental settings.



1. INTRODUCTION

Over the past decade, we have witnessed a tremendous surge of interest in the fundamental studies and applications of gold and silver nanoparticles (AuNPs and AgNPs) as well as nanocrystals (nanostructures with a controlled shape, such as cube, octahedron, triangular plate, pentagonal wire, etc.), which exhibit strong optical absorption and scattering properties in the visible and near-infrared regions of the electromagnetic spectrum.^{1–4} Their unique optical properties have been understood to originate from the localized surface plasmon resonances (LSPRs), i.e., collective resonant oscillations of conduction electrons in these noble metal nanostructures. These localized resonances allow for focus and enhancement of optical energy to subwavelength regions,^{5–11} breaking the diffraction limit based on pure optical means. Previous studies have shown that the LSPRs can be tailored by nanoparticle/nanocrystal composition, size, shape, and local dielectric environment,^{12,13} enabling tailoring of spectral response and applications in plasmonic sensing.¹⁴ Recently, considerable attention has been shifted to the studies of couple pairs (dimers)^{15–17} as well as one-dimensional (1D),^{18,19} two-dimensional (2D),^{20–22} and three-dimensional (3D)^{23,24} nanoparticle/nanocrystal arrays because of their interesting and potentially useful plasmonic coupling properties,^{25,26} which can be implemented in emerging fields of plasmonics,^{5–11} metamaterials (artificially made metal/dielectric composite

materials with feature sizes smaller than the wavelength of light),²⁷ and optical nanoantennas.^{28–30}

In the rapidly developing fields of nanoplasmonics and plasmonic metamaterials, the major concerns are related to internal and external losses in these metal nanostructures. The internal losses are mostly related to the resistive (ohmic) damping (electron–electron scattering, electron–phonon scattering, etc.) and scattering at surfaces, roughness, or defects of metal nanostructures, while the radiative damping results in most of the external losses. Currently, the conventional top-down nanofabrication technique is facing a major challenge in fabricating optical plasmonic metamaterials with sufficient spatial control (size, shape, and lattice) and low energy dissipation due to the limitations of the achievable lateral resolution and the amorphous or polycrystalline nature of evaporated materials. In addition, the surface roughness of the top-down fabricated structures is also a limiting factor. To overcome the difficulties of limited fabrication resolution and internal losses, one promising approach is to utilize high-quality, crystalline metal nanostructures, such as noble metal nanowires and nanoparticles synthesized by chemical meth-

Special Issue: Colloidal Nanoplasmonics

Received: January 16, 2012

Revised: February 27, 2012

Published: February 28, 2012



ods.^{16,19–25,31,32} On the other hand, the radiative damping can be reduced by taking advantage of the dark modes for plasmon excitation and propagation in strongly coupled metal nanostructures.^{15,16,19,33}

Here, we demonstrate two bottom-up routes for fabricating plasmonic structures and metamaterials based on colloidal nanoparticles and nanocrystals. Owing to their well-controlled sizes, shapes, facile surface chemical functionalization, and excellent plasmonic properties in the visible and near-infrared regions, these nanomaterials are suitable building blocks for bottom-up assembled plasmonic metamaterials for optical applications. Especially, we will show that bottom-up self-assembly techniques of colloidal nanoparticles and nanocrystals can be applied to fabricate plasmonic structures with high structural controllability^{16,19} and large-scale ($> \text{cm}^2$) 2D and 3D nanoparticle arrays.^{22,24} These nanoparticle assemblies exhibit unique and designable plasmonic properties, depending on the material composition, size/shape, intergap distance, and the nanoparticle layer number in the case of 3D nanoparticle supercrystals. Therefore, by using these nanoparticle/nanocrystal structures and metamaterials, the fundamental plasmonic effects could be studied in detail under well-prepared experimental settings.

2. EXPERIMENTAL SECTION

2.1. Synthesis of Au Octahedral Nanoparticle. The synthetic procedure for Au octahedra is described below, following the previous report.^{16,34} A 0.4 mL portion of poly(diallyldimethylammonium chloride) (PDDA, $M_w = 400\,000$ – $500\,000$, 20 wt % in H_2O) and a 0.016 mL of 1 M HCl solution were added to 20 mL of ethylene glycol solution in a glass vial. The mixture was magnetically stirred for 1–2 min at room temperature under ambient conditions. A 0.02 mL portion of 500 mM tetrachloroauric acid tetrahydrate (HAuCl_4) aqueous solution was introduced under stirring (the molar ratio of PDDA to $[\text{AuCl}_4]^-$ ions is 50). The bottle containing the as-prepared gold precursor solution was sealed and subsequently heated at $230\text{ }^\circ\text{C}$ in an oil-bath for 60 min. During the reaction process, the color of the gold precursor changed gradually from yellow to colorless in the initial stage and to a reddish color afterward, reflecting the formation of Au nanoparticles. The final product was collected by centrifugation at 14500 rpm and washed repeatedly with pure water for structural characterization and optical property study. After the centrifugation, the products were deposited on the bottom of the tubes, and the supernatant solution became clear and colorless, indicating no Au nanoparticles in the solution.

2.2. Synthesis of Au Nanocubes. Gold nanocubes were synthesized by a two-step seed-mediated growth method.^{19,35} The first seed Au nanocrystals were synthesized by swiftly adding 600 μL of ice-cold 10 mM NaBH_4 aqueous solution to 7.8 mL of an aqueous solution of cetyltrimethylammonium bromide (CTAB, 78 μmol) and $\text{HAuCl}_4 \cdot 4\text{H}_2\text{O}$ (2.5 μmol). The brownish solution containing ~ 4 nm Au nanocrystal solution was obtained after vigorously stirring for 2 min. The second Au nanocube seeds (side length: 43 nm) were synthesized by adding the ~ 4 nm seed solution to the growth solution, following the previous report. The growth solution was prepared by adding 600 μL of 0.1 M L-ascorbic acid aqueous solution to 4.8 mL of an aqueous solution of CTAB (80 μmol) and $\text{HAuCl}_4 \cdot 4\text{H}_2\text{O}$ (1.0 μmol) to form a colorless solution. A 2.5 μL portion of 10-time diluted seed solution was introduced to the growth solution with slow stirring. Storing still at room temperature for 12 h gave the pale red solution containing Au nanocubes with edge size of 43 ± 1.9 nm by the slow reduction of Au^+ to Au^0 . The second Au nanocube seeds were purified by centrifugation. Subsequently, a 400 μL portion of the second seed solution was poured in 28 mL of another growth aqueous solution containing CTAB (800 μmol) and $\text{HAuCl}_4 \cdot 4\text{H}_2\text{O}$ (6.0 μmol) to which 3.6 mL of 0.1 M L-ascorbic acid aqueous solution was added. The large Au nanocubes with edge size of 169 ± 7.0 nm were formed after

1-day growth without stirring. The concentration of second seed dispersion was controlled at 44, 20, 10, 5, 2.3 μM so that their molar ratio to growth solution was changed. A spontaneous precipitation of these large Au nanocubes was used for purification.

2.3. Chemical Synthesis of Colloidal Au Plates. In this synthesis process,^{36–38} 2 mL of ethylene glycol solution of HAuCl_4 (0.033 M) was stirred at $160\text{ }^\circ\text{C}$ in a flask placed on a hot plate. Then 1 mL of ethylene glycol solution of polyvinylpyrrolidone (PVP) was injected in a dropwise fashion. Then, the reaction mixture was continuously stirred at $150\text{ }^\circ\text{C}$ for about 60 min. The solution was then rinsed with deionized water and centrifuged repeatedly to remove the possible residues. Through the solution-phase method, single-crystalline hexagonal and triangular gold plates of several micrometers in lateral size and tens of nanometers in height were synthesized in large quantities.

2.4. Synthesis of Colloidal Au Nanoparticles (6 nm in Core Diameter). We followed a conventional method to prepare water-soluble AuNPs with a uniform size distribution.^{39,40} A 100 mL aqueous solution of gold colloidal nanoparticles (Au colloids) was prepared by mixing 80 mL of chlorauric acid solution (1 mL of 1% HAuCl_4 in 79 mL deionized water) with a 20 mL reducing mixture (1 mL of 4% trisodium citrate, 0.1 mL of 1% tannic acid, and 0.05 mL of 50 mM potassium carbonate in deionized water) at $60\text{ }^\circ\text{C}$ and was maintained for 1 h. Afterward, the synthesized Au colloids were stored at $5\text{ }^\circ\text{C}$.

2.5. Synthesis of Colloidal Ag Nanoparticles (6 nm in Core Diameter).⁴¹ Diethylene glycol (DEG) solution of silver colloidal nanoparticles (Ag colloids) was prepared by mixing 15 mL of poly(acrylic acid) (PAA)/DEG solution (0.81 g PAA + 15 mL DEG) with a 3 mL silver nitrate mixture (0.1 g AgNO_3 + 3 mL DEG) at $245\text{ }^\circ\text{C}$ (the boiling point of DEG) and was maintained for 10 min.

2.6. Synthesis of Octadecanethiolate-Passivated Au and Ag Nanoparticles. Octadecanethiolate-passivated AuNPs were synthesized using a modified two-phase method. In the conventional one-step, two-phase Brust–Schiffrin method⁴² for the synthesis of AuNPs with a protection monolayer of alkanethiolates, the tetrachloroaurate ions ($[\text{AuCl}_4]^-$) in the aqueous solution are transferred to the organic solution using a phase transfer agent and reduced in the presence of reducing agent and thiols. However, the methods of forming gold nanoparticles in the presence of thiols can only synthesize small AuNPs. Moreover, it has been found that as the thiolate chain length increases, the synthesized nanoparticles become more polydisperse. Therefore, we adopted a two-step, two-phase method for synthesizing thiolate-protected AuNPs.⁴³ Briefly, AuNPs were first synthesized by the aforementioned aqueous method, in which AuCl_4^- was reduced by trisodium citrate. The mean diameter of the synthesized AuNPs in aqueous solutions can be controlled from 3 to 17 nm with typical size deviation less than 10%. For this work, we utilized ~ 6 -nm AuNPs to form 3D AuNP supercrystals. In the second step, the aqueous AuNPs were transferred to toluene using tetraoctylammonium bromide (TOAB) as the transfer agent and were capped with octadecanethiolates in toluene. It should be noted that, to transfer larger AuNPs into the toluene phase, it is necessary to heat the mixture at elevated temperatures.²²

To synthesize octadecanethiolate-passivated AgNPs, we adopted a modified polyol process for uniform AgNP size control ranging from several nanometers to ~ 20 nm in diameter.⁴¹ In this study, we chose the conditions for the synthesis of ~ 6 -nm AgNP in order to compare with the results of AuNP supercrystals. In addition, we used the modified two-phase method for the synthesis of thiolate-protected AgNPs. In this step, an AgNP/DEG solution was transferred to toluene using TOAB as the transfer agent, and AgNPs were capped with octadecanethiolates in toluene. Specifically, a 5 mL AgNP/DEG solution was mixed with a 10 mL, 100 mM TOAB/toluene solution, a 10 mL, 100 mM octadecanethiolate/toluene solution, and 25 mL of toluene. The mixture was stirred vigorously for ~ 10 min and stood for 6 h. Then, we removed the bottom DEG solution. Finally, we utilized a centrifuge to purge the octadecanethiolate-passivated AgNP/toluene solution.

2.7. Nanomanipulation Setup. We used a four-probe nanomanipulator (Zyvox, S100) installed in a field-emission scanning electron microscope (FE-SEM, Zeiss, Ultra 55) for nanomanipulation of nanoparticles into plasmonic structures. First, the nanoparticles to be assembled were randomly deposited onto indium tin oxide (ITO)-coated quartz substrates. Subsequently, nanomanipulation was performed in FE-SEM. Each probe can be precisely positioned via a triple-axis stage with precision down to <5 nm.

2.8. Optical Measurement Setup. The measured samples (on ITO-coated quartz substrates) were positioned onto a glass prism. Index-matching silicone oil was placed between the sample and the prism. Scattering light was collected by an optical microscope with a $100\times$ objective lens (Olympus MPLN, NA = 0.9) and a spectrometer (Ocean Optics, QE65000). We recorded the far-field scattering images using a color digital camera (Canon, EOS 1000D).

3. RESULTS AND DISCUSSION

Our assembly methodology is schematically shown in Figure 1. Two kinds of bottom-up techniques are employed here: (1)

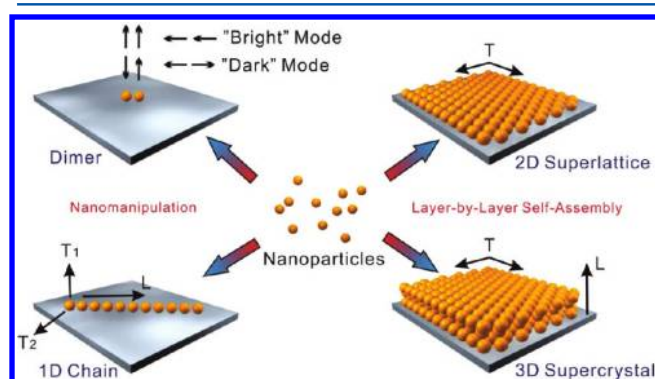


Figure 1. Schematic of the methodology to assemble plasmonic nanostructures and metamaterials composed of gold and silver colloidal nanoparticles (“metaatoms”). To exploit novel, collective plasmonic properties in these structures metamaterials, two kinds of bottom-up assembly techniques are employed, including one-by-one nanomanipulation and large-scale, LbL self-assembly. Due to the strong plasmonic coupling between adjacent nanoparticles, both transverse (T) and longitudinal (L) modes can be controlled by various structural and material parameters, such as particle size/shape, composition, interparticle separation, layer number (for the case of LbL-assembled 3D supercrystal), and so on. In addition, we can excite “dark” or “bright” plasmonic modes by choosing different optical excitation configurations.

nanoparticle/nanocrystal nanomanipulation by applying multiple probes in an FE-SEM and (2) large-scale, layer-by-layer (LbL) self-assembly in liquid phase. These two approaches are complementary to each other. The first approach offers the most versatile way to construct a wide variety of plasmonic nanostructures for a fundamental understanding of plasmonic coupling effects, whereas the second approach is more suitable to fabricate large-scale plasmonic structures for practical applications. It is important to note that the fabrication of large-scale ($> \text{cm}^2$) 2D and 3D nanoparticle arrays is highly desirable in the rapidly developing fields of plasmonic metamaterials. The LbL self-assembly approach offers the unique feature of low-cost, large-scale fabrication for this purpose.

In comparison with single-probe nanomanipulation via scanning probe microscopy,⁴⁴ the FE-SEM-based multiple-probe method offers the following advantages: (1) rapid processing and flexibility in assembling large-scale complicate

structures, (2) 3D simultaneous (“real-time”) observation of the manipulation process, and (3) in situ multiple-probe characterization (e.g., electric and optoelectronic properties) of assembled nanostructure systems. In Figure 2, we show some

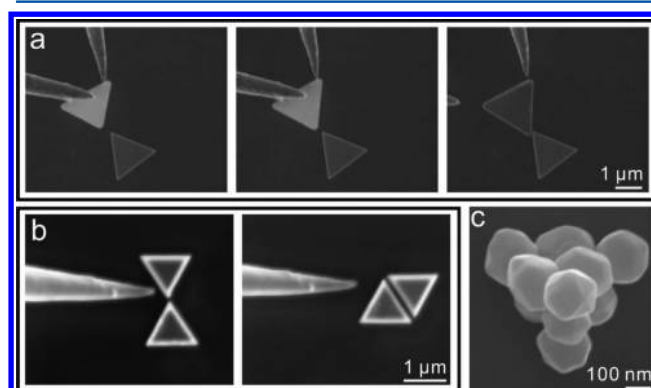


Figure 2. Examples of plasmonic nanostructures assembled by the nanomanipulation technique. The nanomanipulation process was performed in an FE-SEM equipped with a four-probe nanomanipulator. Each probe can be precisely positioned via a triple-axis stage with precision down to <5 nm. This approach allows for simultaneous, real-time imaging and manipulation over large areas. (a) The process of manipulating two single-crystalline gold triangular plates with different tip-to-tip separations. (b) FE-SEM images of a bow-tie nanoantenna and a MIM plasmonic waveguide assembled by using two gold triangular plates. (c) FE-SEM image of a 3D pyramidal structure composed of large colloidal gold nanoparticles, which were one-by-one assembled by using the nanomanipulator.

examples of plasmonic nanostructures assembled from two colloidal Au triangular plates by using the nanomanipulation technique. These structures can be used as bow-tie nanoantenna and metal–insulator–metal (MIM) waveguide for long-range, low-loss plasmon wave propagation. This technique allows us to study many interesting plasmonic structures previously inaccessible by conventional approaches.

To generate the conditions of strong plasmon coupling for noble-metal colloidal nanoparticles, we have recently applied the high-precision nanomanipulation technique for assembly of gold octahedron nanocrystal dimers with tightly controlled interoctahedron nanogaps.¹⁶ Moreover, by studying the gold nanocube chains precisely assembled with adjustable intercube separations, the fundamental properties of dark plasmon propagating modes were revealed in detail under well-prepared experimental settings, such as the number and spacing of nanocubes as well as the incident light direction and scattering light polarization.¹⁹

Figures 3–5 shows the experimental results of plasmonic dimers and plasmonic nanoantenna arrays, demonstrating the uniqueness of our experimental approach. In these optical measurements, the samples to be measured were placed in an optical evanescent field, which was produced by the far-field total internal reflection (TIR) of light (from a 100 W halogen lamp or a supercontinuum fiber laser) using a glass prism, to be measured. Using the TIR measurement geometry, one can control the relative x (in the propagation direction of the evanescent field), y (perpendicular to x , in the substrate plane), and z (in the decaying direction of the evanescent field) components of the TIR-generated evanescent field by adjusting the angle of incidence and polarization. Figures 3 and 5 show the scattering measurements for the coupled plasmon modes

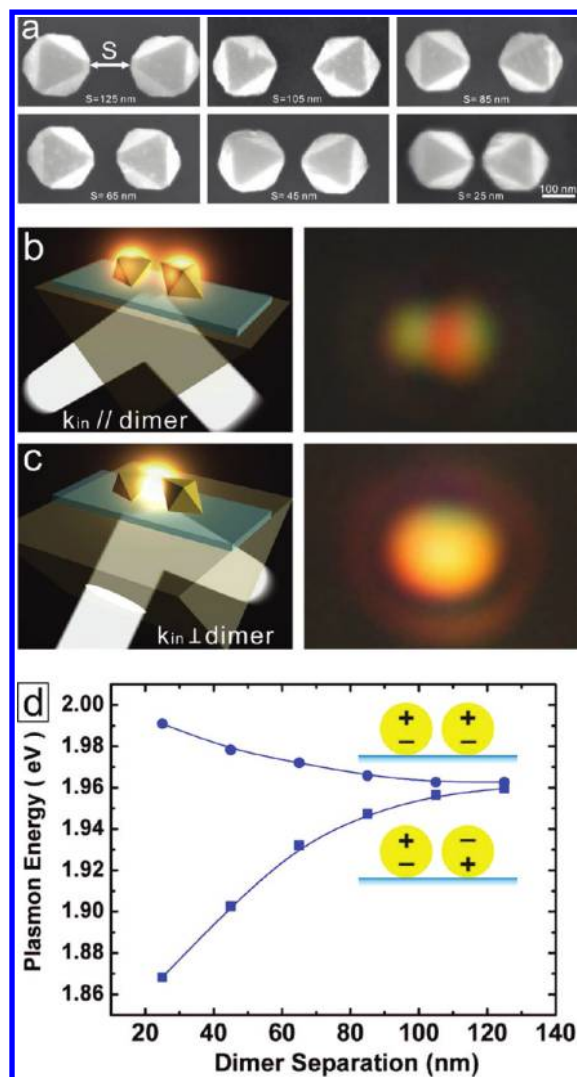


Figure 3. Plasmonic dimers composed of precisely positioned gold octahedra. (a) Using the nanomanipulation technique, two gold octahedral nanocrystals (side length: 150 nm) can be precisely positioned along their major axes with varying tip-to-tip separations (s) on ITO-coated quartz substrates. (b) Schematic of the TIR measurement geometry for observing the plasmonic “dark” mode with antiphase dipole coupling. The TIR-generated evanescent field at an incident angle close to the critical angle excites transversely coupled plasmon modes between two adjacent dipole moments. An actual optical image is shown (tip-to-tip separation: 65 nm) on the right. (c) Schematic of TIR measurement geometry for observing the plasmonic “bright” mode with in-phase dipole coupling. An actual optical image for the same plasmonic dimer is also shown. (d) According to polarization-selective microscattering spectra (scattered light polarization parallel to the incident light wavevector) of octahedral nanocrystal dimers with varying tip-to-tip separations (s : 25–125 nm), the theoretically predicted plasmonic hybridization between noble-metal nanocrystals can be directly confirmed.¹⁶

excited by the transverse magnetic field (TM)-polarized component of the incident light that was irradiated parallel and perpendicular to the dimer axis (Figure 3) and parallel to the chain direction (Figure 5).

It is important to note that, in the TIR excitation geometry at an incident angle close to the critical angle (our measurement condition), the TM-polarized component of the incident evanescent field excites the transverse coupling mode (induced



Figure 4. Gold nanocube chains formed by using the nanomanipulation technique with varying chain lengths and intercube separations. To assemble these chains, we utilized chemically prepared gold nanocubes with a well-defined crystal structure as well as monodispersed size and shape. Large and uniform gold nanocubes (~ 170 nm in side length) were synthesized by a two-step, seed-mediated growth method. The gold nanocubes were randomly deposited onto ITO-coated quartz substrates using a drop-casting technique. Subsequently, the nanocubes were assembled into tip-to-tip chains in an FE-SEM using an in situ four-probe nanomanipulator. By using this technique, we can obtain precisely assembled nanocube chains on ITO-coated quartz substrates with well-separated individual nanocubes, exact nanocube number (chain length), and precisely controlled intercube tip-to-tip separation (in this figure, from left to right, 45–210 nm).

polarizations oriented perpendicular to the dimer or chain axis), instead of the conventional longitudinal coupling mode (induced polarizations oriented parallel to the dimer axis). In the transverse and longitudinal coupling modes, the spectral shifts of coupled plasmon energies with varying nanocrystal separations are in the opposite trend. The assembled gold octahedron nanocrystal dimers with varying tip-to-tip separations (s) are shown in Figure 3a. When the irradiation of the incident light is parallel to the dimer axis (Figure 3b), the optical excitation induces a dark (antiphase dipole coupling) mode in the nanocrystal dimer because of phase retardation, whereas the excitation with the incident direction perpendicular to the dimer axis (Figure 3c) excites a bright (in-phase) mode in the z direction. Figure 3d shows the results of scattering measurements with the incident light wave vector oriented parallel or perpendicular the dimer axis. For the parallel incident light, we found that large red shift of the coupled LSPR peaks occurs when the dimer separation is decreased, which can be attributed to the expected behavior of antiphase plasmon coupling modes in the hybridization model.¹⁵ By contrast, for the scattering spectra taken with the incident light perpendicular to the dimer axis, we found that slight blue shifts of the coupled plasmon resonant peaks occur when the dimer separation is decreased. This results from the in-phase plasmon modes. These results demonstrate that the LSPR wavelength is controllable to a high degree of precision over the visible region via tuning of the localized surface plasmon coupling of two adjacent nanocrystals.

Figure 5a shows a schematic representation of the optical scattering measurement setup in ambient air for characterizing the linear Au nanocube chains shown in Figures 4 and 5b. Samples to be measured were placed in an optical evanescent field produced by the TIR of light (from a 100 W halogen lamp or a supercontinuum fiber laser) using a prism glass. In these measurements, the incident light direction was aligned to be parallel to the chain, and the scattered light was collected

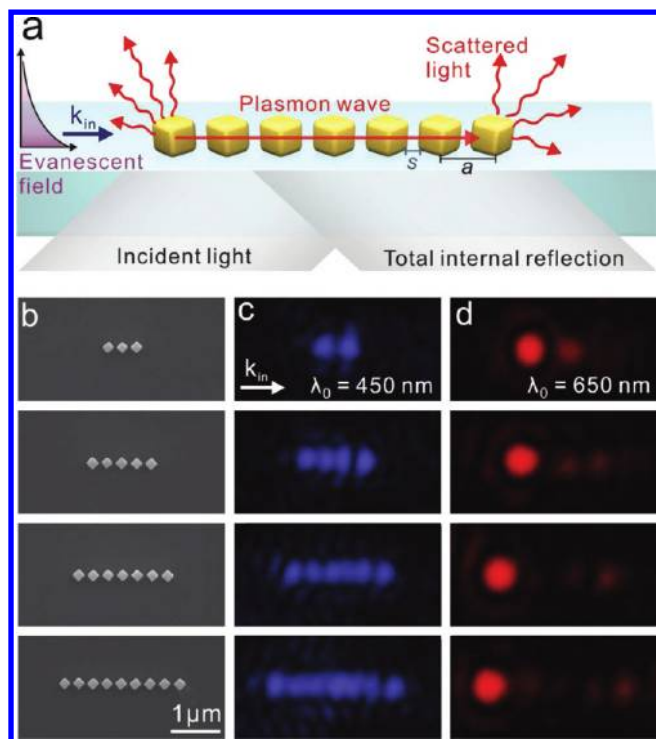


Figure 5. Linear gold nanocube chains as plasmonic nanoantenna arrays. (a) Schematic of the optical scattering measurement setup for a linear chain of plasmon-coupled gold nanocubes. The incident TIR light is directed parallel to the chain, and the collected light passes through a polarizer parallel to the chain axis (longitudinal direction). (b) FE-SEM images showing linear nanocube chains composed of 3, 5, 7, and 9 uniformly spaced nanocubes (nanocube side length: $\sim 170 \text{ nm}$; intercub tip-to-tip separation: $70 \pm 5 \text{ nm}$). (c,d) Corresponding optical scattering images at nonresonant (blue, 450 nm) and resonant (red, 650 nm) incident laser wavelengths. It should be noted that the “dark” plasmon guiding modes only occur for plasmon-coupled chains at resonant wavelength.¹⁹

through a polarizer parallel to the chain axis (longitudinal polarization). This polarization is chosen because it can be related to the plasmon guiding mode, which propagates toward the distal end of the chain. Under near-field plasmon coupling and resonant (free-space wavelength of incident laser at 650 nm, see Figure 5d) conditions, we can clearly observe the occurrence of the dark plasmon propagating mode inside the chain, which exhibits no far-field radiation (and is therefore free from the effects of radiative damping). Figure 5c shows that, under nonresonant (free-space wavelength of incident laser at 450 nm) conditions, the Au nanocubes behave as individual light scattering centers, and the grating effect plays an important role in resulting far-field optical images.¹⁹ In the nonresonant case, radiative damping is very severe, and we do not have the low-loss advantages of dark plasmon modes. From these examples, we can confirm the potential of the nanomanipulation approach for future proof-of-concept experiments to discover novel plasmon coupling effects. For example, to investigate the plasmon-enhanced light–matter interactions, we can incorporate nanomaterials (e.g., semiconductor quantum dots,⁴⁵ nanodiamonds,⁴⁶ etc.) into these plasmonic structures to explore plasmon-enhanced optical processes.

As for large-scale self-assembly of plasmonic metamaterials, we have recently discovered a simple and efficient method for synthesizing large-area ($>1 \text{ cm}^2$), 3D AuNP and AgNP

supercrystal films.²⁴ In this approach, Janus nanoparticle (top face solvent-phobic and bottom face solvent-philic) films with an arbitrary number of close-packed nanoparticle monolayers can be formed using LbL assembly from suspensions of thiolate-passivated AuNPs or AgNPs (see Figure 6). To create

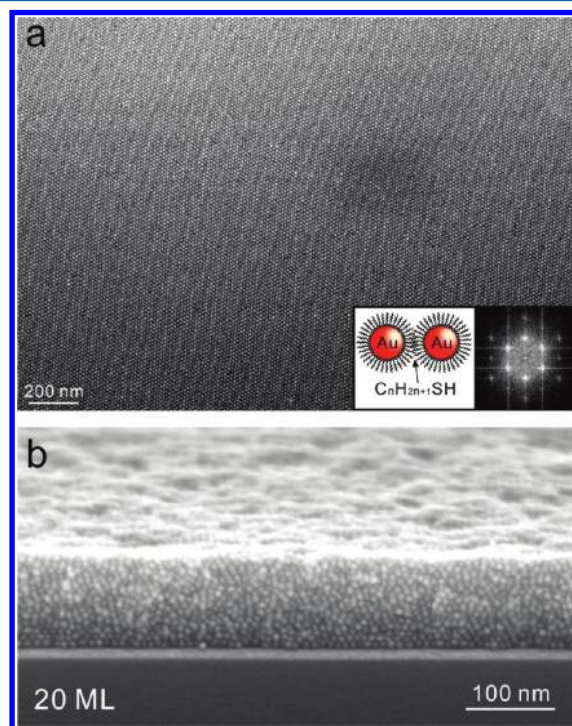


Figure 6. 2D and 3D plasmonic metamaterials formed by LbL self-assembly. (a) FE-SEM image (plan view) of a large-area 2D superlattice self-assembled by octadecanethiolate-stabilized AuNPs ($\sim 10 \text{ nm}$ in diameter) onto a quartz substrate. The deposition process (similar to capillary liquid epitaxy) was performed using a toluene solution of AuNPs. The self-assembled nanoparticle superlattice is highly ordered, as illustrated by the diffraction pattern (fast Fourier transform of a $250 \times 250 \text{ nm}^2$ high-resolution FE-SEM image). In addition, the lattice constant can be tuned by using different carbon chain lengths of nanoparticle surface ligands (alkanethiols, $\text{C}_n\text{H}_{2n+1}\text{SH}$). (b) FE-SEM image (cross sectional view, imaged on a cleaved facet) of a 3D supercrystal LbL self-assembled by octadecanethiolate-stabilized AuNPs ($\sim 6 \text{ nm}$ in diameter) onto a silicon substrate. For the present case, 20 monolayers (ML) of AuNPs are deposited. The layer-forming process can be repeated for arbitrary times to form multilayered films of desired layer numbers.

the Janus nanoparticle monolayers, we applied a simple and scalable air plasma technique⁴⁷ to modify (oxidize) the surfaces of closed-packed, thiol-capped AuNP or AgNP monolayers after every LbL assembly step. We have demonstrated that these films can act as true 3D plasmonic crystals with strong transverse (intralayer) and longitudinal (interlayer) near-field coupling (see Figure 7). In contrast to conventional polyelectrolyte-mediated LbL assembly processes, this approach allows multiple longitudinal coupling modes with a conspicuous spectral dependence on the layer number. We have found a universal scaling relation between the spectral position of the reflectance dips related to the longitudinal modes and the layer number. This relation can be understood in terms of the presence of a plasmonic Fabry–Pérot nanocavity along the longitudinal direction that allows the formation of standing plasmon waves under plasmon resonance

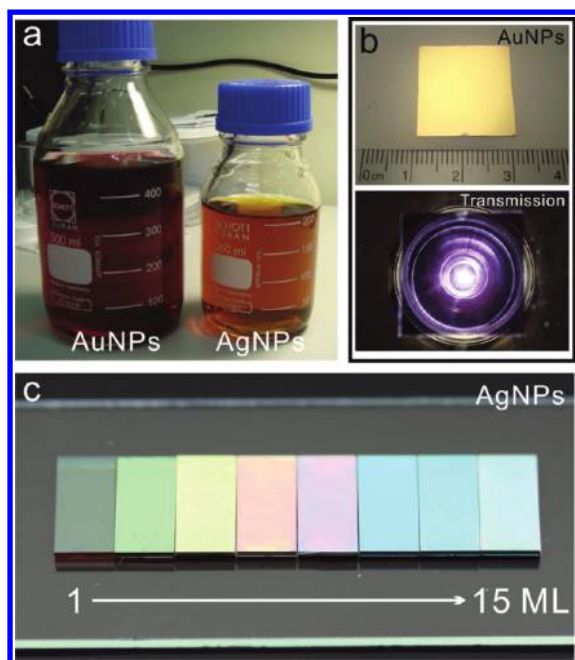


Figure 7. Plasmonic supercrystals assembled from gold and silver colloidal nanoparticles. (a) Aqueous solutions of AuNP and AgNP dispersions with a uniform size distribution (~ 6 nm in mean diameter). For performing LbL self-assembly, the aqueous AuNPs were transferred to toluene and capped with alkanethiolates using a modified two-phase method. (b) Plasmonic response of a large-area ($\sim 2 \times 2$ cm²), highly uniform 10 ML AuNP film on quartz, demonstrating the effects of collective plasmonic resonance. The reflection photograph shows that the plasmonic resonance peak (568 nm) is at greenish-yellow, which makes the AuNP film exhibit a hue similar to that of a sputtered gold film. In contrast, the transmission photograph through the film (illuminated by a halogen light source in combination with a flashlight parabolic reflector) shows that this film has a brilliant purple color, which is drastically different from the original ruby red color of AuNP dispersion. (c) Optical reflection from AgNP (~ 6 nm in diameter) films with thicknesses of 1, 3, 5, 7, 9, 11, and 15 ML. The rainbow-colored photographs result from the combined effect of two plasmonic resonance bands [one constant peak at 468 nm (transverse mode) and another one sensitively depending on the layer number (longitudinal mode)].

conditions. The realization of 3D plasmonic coupling enables broadband tuning of the collective plasmon response over a wide spectral range (visible and near-IR) and provides a pathway to designable plasmonic metamaterials.

In addition, we have found that this LbL self-assembly technique can be used for the fabrication of nanoparticle heterostructures, such as MIM layered plasmonic structures based on these nanoparticle supercrystals stacked with dielectric (e.g., SiO₂, Al₂O₃) interlayers or onto substrates with various metal overlayers. These heterostructures are useful for fundamental studies and applications related to the unusual properties of negative refractive index, slow light, and perfect optical absorption. Furthermore, by utilizing a combined top-down and bottom-up approach, we can design and fabricate plasmonic nanostructures with high flexibility.

4. CONCLUSIONS

We have shown two approaches based on bottom-up assembly to realize 0D (dimers or oligomers), 1D (chain), 2D (superlattice), and 3D (supercrystal) plasmonic structures and metamaterials. These artificially structured nanoparticle/nano-

crystal composites, formed by high-precision nanomanipulation and large-scale self-assembly, exhibit unusual (compared to bulk materials) and designable plasmonic properties. Using these techniques, we can control not only the plasmonic resonance of plasmonic metamaterials over the complete visible and near-infrared spectrum range, but also the subradiant (dark) or superradiant (bright) mode in coupled plasmonic structures. In the case of linearly coupled Au nanocrystal chains, we demonstrate that plasmonic dark modes hold great promise for low-loss subwavelength concentration, manipulation, and transport of light. In the future, these plasmonic structures and metamaterials can be applied for studies and applications requiring unusual optical properties, such as negative refractive index, slow light propagation, and perfect optical absorption.

AUTHOR INFORMATION

Corresponding Author

*E-mail: gwo@mx.nthu.edu.tw.

Notes

The authors declare no competing financial interest.

ACKNOWLEDGMENTS

This study was supported in part by the National Science Council in Taiwan through the National Nanoscience and Nanotechnology Program under Grant No. NSC-100-2120-M-007-001 (S.G.). This study was also partially supported by a KAKENHI Grant-Aid for Scientific Research A (No. 23245028) from the Ministry of Education, Culture, Sports, Science, and Technology (MEXT), Japan (T.T.).

REFERENCES

- (1) Kelly, K. L.; Coronado, E.; Zhao, L. L.; Schatz, G. C. *J. Phys. Chem. B* **2003**, *107*, 668–677.
- (2) Liz-Marzán, L. M. *Langmuir* **2006**, *22*, 32.
- (3) Teranishi, T.; Eguchi, M.; Kanehara, M.; Gwo, S. *J. Mater. Chem.* **2011**, *21*, 10238.
- (4) Rycenga, M.; Cobley, C. M.; Zeng, J.; Li, W.; Moran, C. H.; Zhang, Q.; Qin, D.; Xia, Y. *Chem. Rev.* **2011**, *111*, 3669.
- (5) Barnes, W. L.; Dereux, A.; Ebbesen, T. W. *Nature* **2003**, *424*, 824.
- (6) Maier, S. A.; Atwater, H. A. *J. Appl. Phys.* **2005**, *98*, 011101.
- (7) Stockman, M. I. *Phys. Today* **2011**, *64*, 39.
- (8) Maier, S. A. *Plasmonics: Fundamentals and Applications*; Springer: New York, 2007.
- (9) Gramotnev, D. K.; Bozhevolnyi, S. I. *Nat. Photonics* **2010**, *4*, 83.
- (10) Schuller, J. A.; Barnard, E. S.; Cai, W.; Jun, Y. C.; White, J. S.; Brongersma, M. L. *Nat. Mater.* **2010**, *9*, 193.
- (11) Atwater, H. A.; Polman, A. *Nat. Mater.* **2010**, *9*, 205.
- (12) Link, S.; El-Sayed, M. A. *J. Phys. Chem. B* **1999**, *103*, 4212.
- (13) Underwood, S.; Mulvaney, P. *Langmuir* **1994**, *10*, 3427–3430.
- (14) Anker, J. N.; Hall, W. P.; Lyandres, O.; Shah, N. C.; Zhan, J.; Van Duyne, R. P. *Nat. Mater.* **2008**, *7*, 442.
- (15) Nordlander, P.; Oubre, C.; Prodan, E.; Li, K.; Stockman, M. I. *Nano Lett.* **2004**, *4*, 899.
- (16) Yang, S.-C.; Kober, H.; He, C.-L.; Lin, M.-H.; Chen, H.-Y.; Li, C.; Kanehara, M.; T. Teranishi, T.; Gwo, S. *Nano Lett.* **2010**, *10*, 632.
- (17) Nabika, H.; Takase, M.; Nagasawa, F.; Murakoshi, K. *J. Phys. Chem. Lett.* **2010**, *1*, 2470.
- (18) Maier, S. A.; Kik, P. G.; Atwater, H. A.; Meltzer, S.; Harel, E.; Koel, B. E.; Requicha, A. A. G. *Nat. Mater.* **2003**, *2*, 229.
- (19) Chen, H.-Y.; He, C.-L.; Wang, C.-Y.; Lin, M.-H.; Mitsui, D.; Eguchi, M.; Teranishi, T.; Gwo, S. *ACS Nano* **2011**, *5*, 8223.
- (20) Ung, T.; Liz-Marzán, L. M.; Mulvaney, P. *J. Phys. Chem. B* **2001**, *105*, 3441–3452.
- (21) Tao, A. R.; Sinsermsuksakul, P.; Yang, P. *Nat. Nanotechnol.* **2007**, *2*, 435.

- (22) Chen, C.-F.; Tzeng, S.-D.; Chen, H.-Y.; Lin, K.-J.; Gwo, S. *J. Am. Chem. Soc.* **2008**, *130*, 824.
- (23) Tao, A. R.; Ceperley, D. P.; Sinsermsuksakul, P.; Neureuther, A. R.; Yang, P. *Nano Lett.* **2008**, *8*, 4033.
- (24) Lin, M.-H.; Chen, H.-Y.; Gwo, S. *J. Am. Chem. Soc.* **2010**, *132*, 11259.
- (25) Prodan, E.; Radloff, C.; Halas, N. J.; Nordlander, P. *J. Science* **2003**, *302*, 419.
- (26) Halas, N. J.; Lal, S.; Chang, W.-S.; Link, S.; Nordlander, P. *Chem. Rev.* **2011**, *111*, 3913.
- (27) Cai, W.; Shalaev, V. *Optical Metamaterials: Fundamentals and Applications*; Springer: New York, 2010.
- (28) Mühlischlegel, P.; Eisler, H.-J.; Martin, O. J. F.; Hecht, B.; Pohl, D. W. *Science* **2005**, *308*, 1607.
- (29) Novotny, L.; van Hulst, N. *Nat. Photonics* **2011**, *5*, 83.
- (30) Giannini, V.; Fernández-Domínguez, A. I.; Heck, S. C.; Maier, S. A. *Chem. Rev.* **2011**, *111*, 3888.
- (31) Ditlebacher, H.; Hohenau, A.; Wagner, D.; Kreibig, U.; Rogers, M.; Hofer, F.; Aussenegg, F. R.; Krenn, J. R. *Phys. Rev. Lett.* **2005**, *95*, 257403.
- (32) Huang, J.-S.; Callegari, V.; Geisler, P.; Brüning, C.; Kern, J.; Prangma, J. C.; Wu, X.; Feichtner, T.; Ziegler, J.; Weinmann, P.; Kamp, M.; Forchel, A.; Biagioni, P.; Sennhauser, U.; Hecht, B. *Nat. Commun.* **2010**, *1*, 150.
- (33) Liu, M.; Lee, T.-W.; Gray, S. K.; Guyot-Sionnest, P.; Pelton, M. *Phys. Rev. Lett.* **2009**, *102*, 107401.
- (34) Li, C.; Shuford, K. L.; Chen, M.; Lee, E. J.; Cho, S. O. *ACS Nano* **2008**, *2*, 1760.
- (35) Sau, T. K.; Murphy, C. J. *J. Am. Chem. Soc.* **2004**, *126*, 8648.
- (36) Sun, Y. G.; Xia, Y. N. *Science* **2002**, *298*, 2176.
- (37) Kan, C. X.; Zhu, X. G.; Wang, G. H. *J. Phys. Chem. B* **2006**, *110*, 4651.
- (38) Wu, C.-Y.; He, C.-L.; Lee, H.-M.; Chen, H.-Y.; Gwo, S. *J. Phys. Chem. C* **2010**, *114*, 12987.
- (39) Turkevich, J.; Stevenson, P. C.; Hillier, J. *Discuss. Faraday Soc.* **1951**, *11*, 55.
- (40) Slot, J. W.; Geuze, H. J. *Eur. J. Cell Biol.* **1985**, *38*, 87.
- (41) Hu, Y.; Ge, J.; Lim, D.; Zhang, T.; Yin, Y. *J. Solid State Chem.* **2008**, *181*, 1524.
- (42) Brust, M.; Walker, M.; Bethell, D.; Schiffrin, D. J.; Whyman, R. *J. Chem. Soc., Chem. Commun.* **1994**, 801.
- (43) Tzeng, S.-D.; Lin, K.-J.; Hu, J.-C.; Chen, L.-J.; Gwo, S. *Adv. Mater.* **2006**, *18*, 1147.
- (44) Benson, O. *Nature* **2011**, *480*, 193.
- (45) Wei, H.; Ratchford, D.; Li, X.; Xu, H.; Shih, C.-K. *Nano Lett.* **2009**, *9*, 4168.
- (46) Schietinger, S.; Barth, M.; Aichile, T.; Benson, O. *Nano Lett.* **2009**, *9*, 1694.
- (47) Lin, M.-H.; Chen, C.-F.; Shiu, H.-W.; Chen, C.-H.; Gwo, S. *J. Am. Chem. Soc.* **2009**, *131*, 10984.